PAPER

Check for updates

The emergence of MnFe$_2$O$_4$ nanosphere-based humidity sensor: a methodical investigation by scanning Kelvin probe and its deployment in multitudinous applications†

Rahul S. Ghuge,[a] Manish D. Shinde,[b] V. Hajeesh Kumar,[c] Sudhir S. Arbuj, [iD][b]
Velappa Jayaraman Surya, [iD][de] Sunit B. Rane,*[b] Corrado Di Natale[f] and
Yuvaraj Sivalingam [iD] *[ag]

In this study, the ambient temperature humidity sensing properties of solvothermally synthesized MnFe$_2$O$_4$ (MFO) nanospheres on interconnected comb-like silver electrodes were studied systematically. The sensing results revealed that the resistance of MFO decreased as the relative humidity (RH) increased owing to negative RH sensing characteristics. The prepared spinel-structured MFO sensor exhibited a wide humidity detection range (11% to 85% – static method), low hysteresis (~5%) between the adsorption and desorption curves, high sensitivity (1.930 MΩ/%RH) and excellent detection resolution (2% RH). A scanning Kelvin probe (SKP) system was used to investigate the influence of different percentages of RH conditions on the surface potential of the sensor. The results showed that humidity directly affected the material's work function (ϕ) and contact potential difference (CPD). Finally, the fabricated sensor was integrated and tested in real-time samples, such as baby diapers, finger humidity for contactless switches, sweat pads, human breath for breath analysis/monitoring, and skin for the detection and monitoring of moisture levels.

[a] *Laboratory of Sensors, Energy and Electronic Devices (Lab SEED), Department of Physics and Nanotechnology, SRM Institute of Science and Technology, Kattankulathur 603203, Tamil Nadu, India. E-mail: yuvarajs2@srmist.edu.in*

[b] *Centre for Materials for Electronics Technology, Off Pashan Road, Panchawati, Pune 411008, India. E-mail: sunit@cmet.gov.in*

[c] *Functional Coatings and Materials Laboratory, Department of Physics and Nanotechnology, SRM Institute of Science and Technology, Kattankulathur 603203, Tamil Nadu, India*

[d] *Novel, Advanced, and Applied Materials (NAAM) Laboratory, Department of Physics and Nanotechnology, SRM Institute of Science and Technology, Kattankulathur 603203, Tamil Nadu, India*

[e] *New Industry Creation Hatchery Center (NICHe), Tohoku University, Aoba-ku, Sendai 980-8579, Miyagi, Japan*

[f] *Department of Electronic Engineering, University of Rome Tor Vergata, Via del Politecnico 1, 00133 Roma, Italy*

[g] *Sensors Lab, Advanced Membranes & Porous Materials Center (AMPM), Computer, Electrical and Mathematical Science and Engineering Division (CEMSE), King Abdullah University of Science and Technology (KAUST), Thuwal 23955-6900, Kingdom of Saudi Arabia. E-mail: yuvaraj.sivalingam@kaust.edu.sa*

† Electronic supplementary information (ESI) available: Schematic illustration of Scanning Kelvin Probe System (SKP), sensitivity curve, static sensor response with standard salts, sensing response under the influence of different components, such as wet/dry tissue paper, with/without hand gloves, dry/wet finger and hand palm, the device fabrication process for baby diaper alarm, comparison of the sensor with earliest ferrite-based sensors. See DOI: https://doi.org/10.1039/d3ma00694h

1. Introduction

Recently, humidity sensors have aroused great attention in various sectors, including industries to control short-circuits,[1,2] healthcare for breath analysis/monitoring,[3–8] agriculture for the forecasting of weather information and to test plant transpiration systems[9,10] and many other fields. Concerning their extreme necessity in varied areas, it is imperative to develop cost-effective susceptible humidity sensors to monitor, identify, and regulate ambient humidity. The literature survey has inferred that good-quality humidity sensors possess high sensitivity, swift responsivity, reproducibility, negligible aging effect, low response/recovery time, stability, and high resolution.[11–13] In general, humidity sensing is a surface phenomenon whose performance greatly influences various internal and external parameters, such as the structural properties of sensor materials, their surface-to-volume ratio, the microstructure of the sensing layer, surface additives, and temperature.[14] Changes in capacitance,[3,5,9,11] current,[10,12] impedance,[9,13,15] optical intensity,[16] and frequency[17,18] are the explored transduction mechanisms for humidity sensing. Water polarization directly affects the material's conductivity; hence, resistance-based sensing constitutes the major chunk of commercially available humidity sensors and has been acknowledged as a more straightforward,

effortless, and primary method among those parameters. The type of materials (either n-type or p-type) assigns the positive or negative change in resistance with respect to relative humidity (RH); for p-type materials, the resistance values increase with % RH and *vice versa* for n-type materials.[12,14,19]

To enrich the ever-evolving demands across multiple fields of applications, numerous studies have been devoted to hybrid, organic and inorganic semiconducting material families. Ferrite is one of the members of the inorganic material family containing binary metallic groups with a high density of active sites for the dissociation of water molecules.[20,21] In particular, $MnFe_2O_4$ (MFO) is a multifunctional ferrite that has intriguing properties, such as versatility in shape and biocompatibility.[22] Hitherto, MFOs with distinct morphologies, such as hollow nanocubes,[23] hollow spheres,[24] octahedrons,[25] nanoparticles,[26] mesoporous microspheres,[27,28] and nanorods,[29] have emerged using copious scientific and engineering techniques to deploy in various applications, such as photocatalysis, biomedical (especially for drug delivery), supercapacitor, and batteries. The microsphere has a high packing density and good mobility to form a uniform and compact layer; thus, it is recognized as an excellent morphology for making electrodes or films.[27,30]

To the best of our knowledge, MFO is yet to be explored for humidity-sensing applications. Interestingly, its high surface area, abundant active sites, excellent electrochemical properties and magnetic properties have been extensively studied owing to their several purposes, including gas sensing.[24–29,31–35] MFO is composed of two phases: first normal spinel MFO, which constitutes divalent Mn^{2+} ions (A) and trivalent Fe^{3+} ions (B) located at tetrahedral and octahedral sites and has the general formula $Mn[A]Fe_2[B]O_4$; and second, inverse spinel, where Mn^{2+} cation (A) occupies the octahedral sites and Fe^{3+} (B) is equally distributed to tetrahedral and octahedral sites with the general formula $Fe[A](MnFe)[B]O_4$.[32,36] Additionally, the spinel structure contains an octahedral framework, a high density of vacancies, and positively charged metal ions, attracting large amounts of water molecules, which is, in turn, beneficial for humidity sensors.[37]

The interaction of humidity on the surface causes an increase or decrease in the number of charge accumulation concentrations on the surface, which subsequently affects the band bending factor and overall conduction.[38] Thus, it is essential to know the effect of different humidity conditions on the electronic properties of sensor materials, such as contact potential difference (CPD) and work function (ϕ). Few studies have employed a scanning Kelvin probe (SKP) approach to examine humidity-dependent ϕ. SKP is a well-established, non-contact, and non-destructive ϕ determination method recently employed in various gas sensing applications.[38–41]

This work demonstrated the humidity-sensing properties of solvothermally synthesized agglomerated MFO nanospheres. MFO possesses excellent biocompatibility, which makes it an attractive option for respiratory monitoring, skin moisture monitoring, and infant diaper wetness monitoring. Additionally, it is inexpensive and easy to manufacture, making it suitable for cost-sensitive commercial applications. Herein, the fabricated MFO sensor was tested in diverse RH ranges *via* dynamic and static sensing routes. The influence of moisture on surface electronic properties, such as CPD and ϕ, was investigated at medium RH (MRH), laboratory RH (LRH) and high RH (HRH) using the SKP system. Further, the humidity sensing mechanism was explained elaborately with the band bending configuration. Finally, the fabricated MFO humidity sensor was successfully used in multiple applications, such as baby diaper alarms, human respiration monitoring, contactless doorbells, sweat pad moisture and skin humidity monitoring. In addition, the sensor response was compared to commercially available HygroClip 2 advanced series HC2A-S.

2. Experimental

2.1 Materials

All the analytical grade chemicals, namely manganese dichloride ($MnCl_2 \cdot 4H_2O$), ferric chloride ($FeCl_3 \cdot 6H_2O$), ethylene glycol ($C_2H_6O_2$), and sodium acetate (CH_3COONa) were used as received without any further purification.

2.2 Synthesis of the MFO-agglomerated microsphere

For typical synthesis, 3.6 g sodium acetate was first dissolved in 40 ml of ethylene glycol. To this solution, 2.5 mmol of $MnCl_2 \cdot 4H_2O$ and 5 mmol of $FeCl_3 \cdot 6H_2O$ were subsequently added with continuous stirring. After 30 min of stirring, the formed transparent yellowish solution was transferred to a Teflon container with a 100 ml capacity. Further, the Teflon container was kept in a stainless steel autoclave and heated at 200 °C for 8 h in an oven. After completion of the reaction, the Teflon vessel was cooled to room temperature naturally. The obtained product was washed with deionized water several times and finally with ethanol and thereafter dried in an oven at 60 °C for 12 h. The obtained MFO powder was grounded in a mortar pestle and used for further study.

2.3 Sensor fabrication

For sensor fabrication, the interdigitated comb-like Ag electrodes (on an alumina substrate with dimensions 0.5 cm × 1 cm and finger distance of 100 μm) were drop casted with water-based MFO dispersion (MFO : H_2O = 0.5 g : 1 ml); however, binder solution was not used during the fabrication to avoid carbon impurities after heating. Finally, the casted film was dried at 60 °C for ~10 min to prevent peeling/crust and then was heated at 350 °C for ~5 h.

2.4 Characterization techniques and sensor parameters

The structural properties of solvothermally synthesized MFO were studied between 2θ range of 10 to 80° at a scanning speed of 2° min^{-1} using a Bruker AXS D-8 X-ray diffractometer, which was equipped with a monochromator and Ni-filtered Cu-K$_\alpha$ radiation. The light absorption properties of the prepared material were studied from 400 to 700 nm using a Shimadzu UV-VIS-NIR spectrophotometer: model UV-3600 in diffuse reflectance spectra (DRS) mode. Surface morphology and size distribution were analysed using field emission scanning

electron microscopy (FESEM, HITACHI S-4800 and NOVA NANOSEM-450). The contact angle measurement was performed on DMs-401 (Kyowa Interface Co., Ltd, Japan). CPD and ϕ measurements were performed using SKP5050 (KP Technology, UK). The current–voltage (I–V) characteristics from -5 V to $+5$ V were studied using the Keithley 4200A SCS semiconductor characterization system with a fixed step size of 0.2 V and a compliance current of 100 mA. Keysight 3472A data acquisition unit was employed for the sensor measurement. The sensing chamber humidity was confirmed using the high-precision HygroClip 2 advanced series HC2A-S, while for SKP chamber humidity confirmation, a standard Testo 410-2 – Vane anemometer was utilized. All measurements were performed at room temperature (25 °C), which was controlled by an air conditioner (AC). In our case, the sensing response was measured using the following equation:[42]

$$R = \left\{ \frac{RH1 - RH2}{RH1} \right\} \times 100, \quad (1)$$

where RH1 is the resistance value at 20% RH and RH2 is the resistance value at a higher RH. The sensitivity of the sensor is calculated using the following relation:[43]

$$S = \frac{\text{Change in an resistance}(\Delta R)}{\text{change in RH}(\Delta \% RH)}. \quad (2)$$

Then, we investigated the selectivity test by comparing the sensitivity of VOCs (acetone (99%), ammonia (25%), ethanol (99%), triethyl amine (TEA), and n-butanol (99.5%)) with humidity. For this purpose, synthetic (dry) air was blown through the relevant liquids to be enriched with the analytes and injected into the sensing chamber at a varied percentage of flow rate controlled by highly accurate mass-flow controllers (Alicat Scientific). The vapour pressure (VP) of all VOCs was evaluated using the following Antoine's equation:[39]

$$\log_{10}(\text{Pi}) = A - \frac{B}{C + T}, \quad (3)$$

where A, B, and C are Antoine constants available at the NIST database,[39] and T is the temperature in Celsius (T is 25 °C). The dynamic measurement ranges used for acetone, ammonia, ethanol, TEA, n-butanol and H_2O were 3000–12 000 ppm, 6800–54 700 ppm, 1500–10 500 ppm, 1600–9800 ppm, and 350–1400 ppm, respectively.

2.5 Sensor characteristics and SKP measurement

The performance of the fabricated sensor was studied in a self-made sensor testing system, as shown in Fig. 1. The dynamic sensing tests were carried out in a 1.6 L stainless steel chamber. The dynamic humidity sensor results were further validated by measuring the sensor response statically. For static sensor measurement, we used saturated solutions of standard humidifier salt, such as LiCl (11%), CH_3COOK (23%), $MgCl_2$ (33%), K_2CO_3 (43%), NaBr (57%), NaCl (75%), KCl (85%) and KNO_3 ($\sim$95%). Detailed measurement information has already been reported in the literature.[42,44] Before sensor measurement, all salts were kept in closed borosilicate glass vessels at 25 °C for
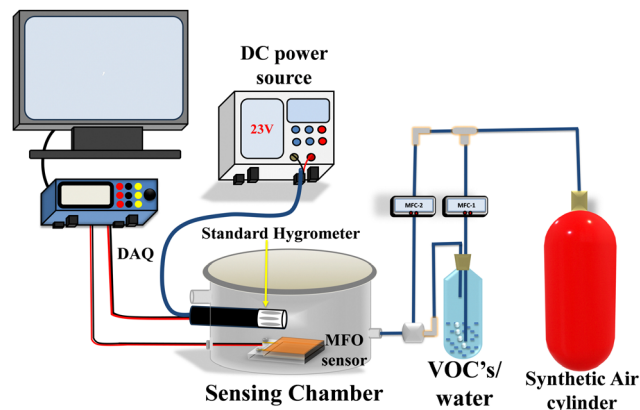

Fig. 1 Schematic diagram of the dynamic humidity sensing system.

$\sim$15 h. Finally, using the same saturated solutions, the I–V characteristics were analysed at different humidities.

Single-point and 3D raster scan CPD measurements were performed using dynamic and static methods, respectively. The dynamic single point CPD measurement was carried out by varying the SKP chamber humidity from $\sim$48% to $\sim$90%, and the static 3D raster scan CPD measurement was done at laboratory RH ($\sim$65%) (LRH), medium RH (50% ($\pm$3)) (MRH), and high RH (90% ($\pm$3)) (HRH). A raster scan was performed in a 90×90 μm^2 area of the film along the X and Y axes. A schematic illustration of the SKP measurement setup is depicted in Fig. S1 (ESI†). The working mechanism of SKP has been described in previous reports.[41,45–47]

3. Results and discussion

3.1 Characterization of the MFO and humidity sensor

The structural and crystallographic data were obtained through XRD analysis (Fig. 2(a)). The presence of diffraction peaks at $2\theta = 29.67, 34.86, 36.5, 42.35, 42.40, 52.63, 56.04, 61.5°$ corresponding to the (220), (311), (222), (400), (422), (511) and (440) planes confirmed the complete simple cubic spinel phase formation of MFO. The diffraction peaks are exactly indexed as ICDD no. 38-0430. The peak corresponding to (311) indicates the formation of highly crystalline nanostructures. No shift within the planes or presence of impurity peaks was noted, which may be attributed to the complete reaction formation. The average crystallite size ($\sim$20.85 nm) was estimated at the (311) plane using the Scherrer equation. Fig. 2(b) and (c) show morphological and topographic images of prepared MFO powder at low and high magnification, respectively. The synthesized MFO possesses uniformly distributed and agglomerated spherical nanoparticles. Microsphere size distribution ranges from 0.1 μm to 0.25 μm with a peak at 0.17 μm (Fig. 2(d)). Optical absorption spectra were recorded using a UV-Vis absorption spectrophotometer in DRS mode, and the corresponding absorption edge was $\sim$730 nm (Fig. 2(e)). The optical band gap energy was estimated to be 2.1 eV using a Tauc plot, as shown in Fig. 2(f). The time-dependent contact angle measurement and I–V characteristics at various RH percentages
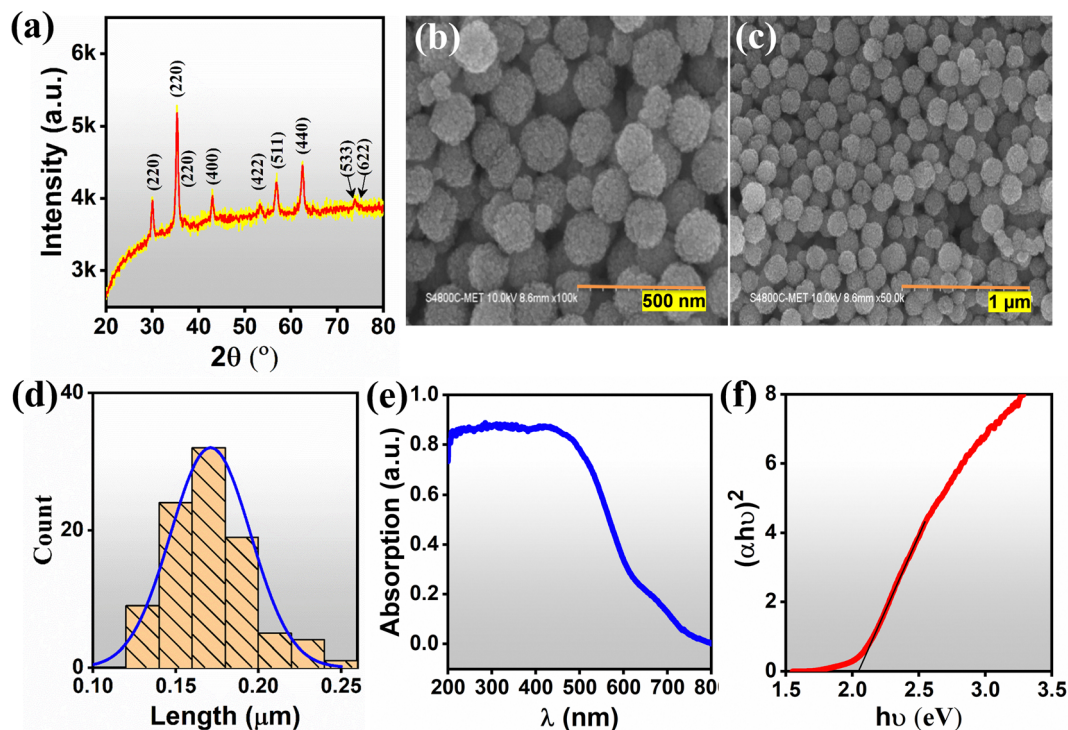
Fig. 2 (a) XRD pattern, (b), (c) FESEM images, (d) particle size distribution, (e) UV-DRS spectra and (f) Tauc plot of synthesized $MnFe_2O_4$.

were carried out to clarify the hydrophilicity and conductivity of the MFO films, respectively (Fig. 3). The results of the former revealed that at the initial stage (<1 s), the contact angle of the MFO film was 22.7°, and then, it decreased to 18.9° in 10 s and to 17.4° in 60 s, respectively (Fig. 3(a)). The MFO microspheres exhibited a highly hydrophilic nature. This is because, in all stages, the estimated contact angles were less than 90°.[7,12] Additionally, only 20 s were required for the contact angle to decrease from 22.7 (beginning stage) to 17.6 (steady stage). Furthermore, the I–V characteristics curve at different humidity conditions revealed variations in the conductivity of the sensor with respect to % RH (Fig. 3(b)). Using Ohm's law ($V = IR$), the estimated resistance values for 11%, 43%, 65% 75%, and 85% RH are calculated to be 120 MΩ, 12.7 MΩ, 1.70 MΩ, 883 kΩ, and

567.3 kΩ, respectively, evincing that electrical conduction has increased with the percentage of RH.

3.2 Humidity sensing performance

Fig. 4(a) shows that the dynamic humidity sensing response curve of the MFO humidity sensor increases the percentage of RH from 20 to 70%. It is noteworthy that, while increasing the concentration of humidity, the resistance value gradually decreased, which confirmed that the sensor exhibited negative sensing properties.[12,48] The functional relationship between the response and RH (20–70%) followed the cubic polynomial fitting (Fig. 4(b)). Additionally, the sensor followed the linear fitting function $y = 3.70x - 77.7$ between the humidity ranging from 20 to 35% (the inset of Fig. 4(b)). Further, a wide range
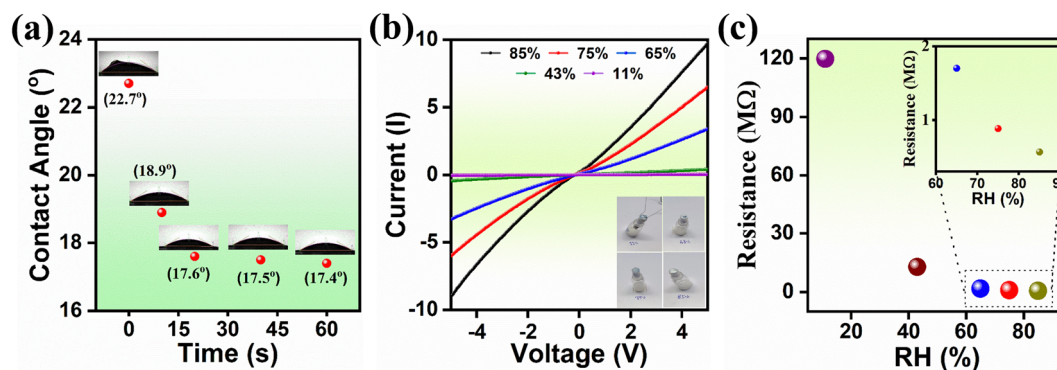

Fig. 3 (a) Time-dependent contact angle measurement, (b) I–V characteristics at various humidities, and (c) corresponding change in resistance with respect to RH.
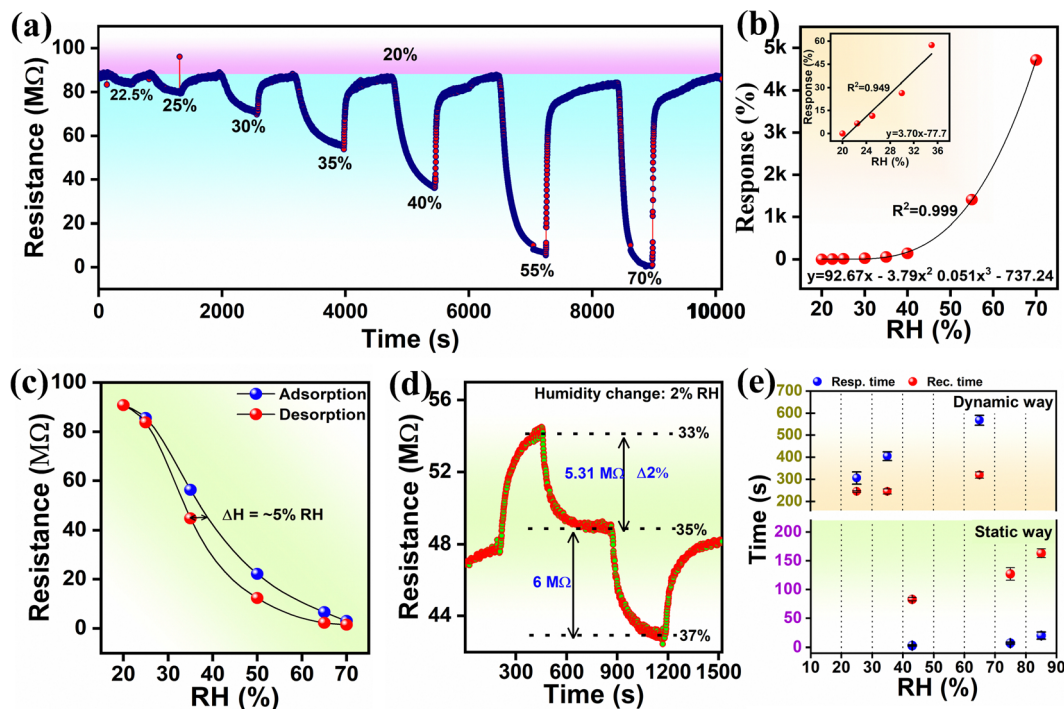
Fig. 4 (a) Dynamic response curve of the humidity sensor to increase relative humidity from 20% to 70%, (b) response as a cubic polynomial fitting function of RH (20–70%), and inset is the linear fitting, (c) hysteresis loop of the sensor during adsorption and desorption of humidity, (d) response curve of the sensor to 2% change of RH, and (e) average response–recovery time by dynamic (at 25%, 35% and 65% RH) and static (at 44%, 75% and 85%, respectively) path.

static sensing test showed an obvious response from 11 to 95% RH, revealing its wide sensing range, and it is noteworthy that baseline drift was negligible towards all humidity concentrations (Fig. S2a and b, ESI†). MFO showed a consistent sensing response towards each humidity level in dynamic and static methods (Fig. S2b, ESI†).

In dynamic sensing, the hysteresis occurring during adsorption and desorption was found to be 5% at a relative humidity of 35% (Fig. 4(c)). Using a static sensing path, the hysteresis error was further examined and found to be reduced to ∼4.2% (Fig. S2c, ESI†). This hysteresis may occur owing to the superhydrophilic nature of MFO. Additionally, in both static and dynamic studies, the sensitivity in the primary region (20–65% RH) was higher than that in the later region, which may be attributed to less proton hopping in the distant layer owing to the less van der Waals force between metal ions and the water layer[49–51] (Fig. S2b, ESI†). By measuring the resistance change with a 2% change in humidity, the high RH resolution sensing capability was proven (Fig. 4(d)). As the percentage of RH decreased from 35% to 33%, the resistance value increased by 5.31 MΩ. Conversely, when RH increased from 35% to 37%, the resistance of the sensor decreased by ∼6 MΩ. The humidity sensor showed good response and recovery characteristics to a 2% RH change, demonstrating its excellent detection resolution experimentally. According to the response-recovery time definition of the humidity sensor,[12] the time lengths required to reach 90% change of the total resistance value during adsorption (70% RH) and desorption (20% RH) were ∼568 s and ∼320 s,

respectively (Fig. 4(e)-top). The response-recovery time was found to be quite higher, which might be due to the large volume of the sensing chamber (∼1.6 L).

For further confirmation, the response/recovery time was further evaluated using a static measurement path. For this, the sensor was alternately switched through various humidity salt cells (such as 43%, 75%, and 85% RHs) with respect to 11% RH (Fig. S3, ESI†). The average response-recovery time between 11% and 85% RH was 20 s and 163 s, respectively (Fig. 4(e)-down). The average response-recovery time between 11% and 85% RH was 20 s and 163 s, respectively (Fig. 4(e)-down), indicating that the sensor chamber size significantly influenced the sensor response. Sensor repeatability was tested for three cycles at three different humidity levels. The test was performed using the dynamic (for 25%, 35% and 65% RH) method and static (43%, 75% and 85%) method, and the resultant response curves showed stable responses, indicating good repeatability (Fig. 5(a) and Fig. S3, ESI†). Fig. 5(b) demonstrates the response constancy for a week. The sensor showed a stable response at lower (20%) and higher (65%) concentrations of RH. However, at 30% and 40% RH, it exhibited quite a deflection.

Interestingly, there have been no reports on MFO-based humidity sensors. Therefore, we compare our results with previous ferrite-based humidity sensors only. A comparison of our results with the other ferrite-based humidity sensors (Table S1, ESI†) affirmed that the MFO-based humidity sensor has covered a comparable and wide range of humidity concentrations, and thus can be deployable in multiple applications. Here, for long-
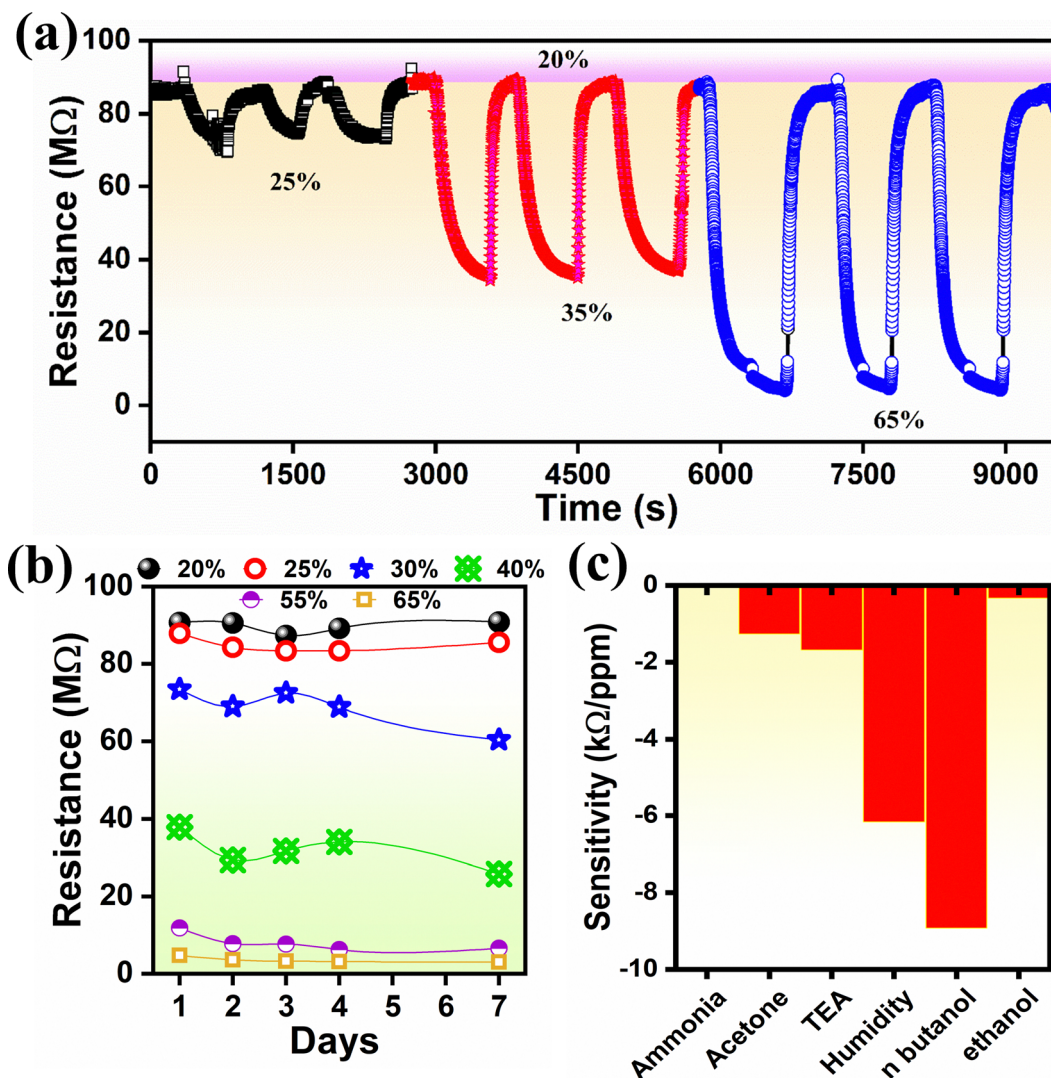
Fig. 5 (a) Repeated response for three cycles at 25, 35, and 65% RH, (b) stability for 7 days, and (c) selectivity test with other volatile organic compounds.

term stability, the humidity sensor needs to be further improved using measures such as high-grade gold electrodes and packing protection. The selectivity test revealed that *n*-butanol has a high sensitivity, which is followed by humidity; however, human breath contains a negligible concentration of *n*-butanol compared to humidity (Fig. 5(c)).

Fig. 6(a) displays the RH-dependent CPD curve. The CPDs were found to be ~325 mV and ~380 mV at ~50% RH and ~90% RH, respectively. Further, the 3D raster scan CPD was performed in LRH, MRH and HRH (Fig. 6(b)). The average CPD values were obtained to be 315 mV, 341 mV, and 374 mV at MRH, LRH, and HRH, respectively. The 3D raster scan results are more consistent with the dynamic single-point CPD results. The average estimated ϕ values were found to be ~5.37 ($\pm$0.0084) eV, ~5.40 ($\pm$0.012) eV, and ~5.43 ($\pm$0.0085) eV for MRH, LRH, and HRH, respectively. Fig. 6(c)–(e) show the corresponding 2D raster scan images at MRH, LRH, and HRH, respectively. A graphical representation of change in ϕ with respect to RH's is shown in Fig. 6(f) and is

enough to make a difference in ϕ under various humidity conditions.

3.3 Sensing mechanism and band bending configuration

Whenever the percentage of RH increases, H_2O molecules cause the surface electric resistance of MFO to decrease by increasing the concentration of electrons *via* two routes:

(i) The reaction of water molecules with surface adsorbed ionized oxygen species (O^-, O^{2-} or O_2^- (superoxide species)) leads to the return of electrons back to the depletion region of MFO,[51–53] (electrostatic conduction) (Fig. 7(a)) and

(ii) attraction of electrons to the surface through surface-absorbed water molecules[51,54] (conduction due to protonic hoping) (Fig. 7(b)–(d)).

Under the initial condition, owing to the polar nature of water molecules, negatively charged oxygen species of water molecules are attracted towards the positively charged metal ions (M) by an electrostatic force. The surface pre-adsorbed superoxides (O_2^-) cause significant dissociation of water
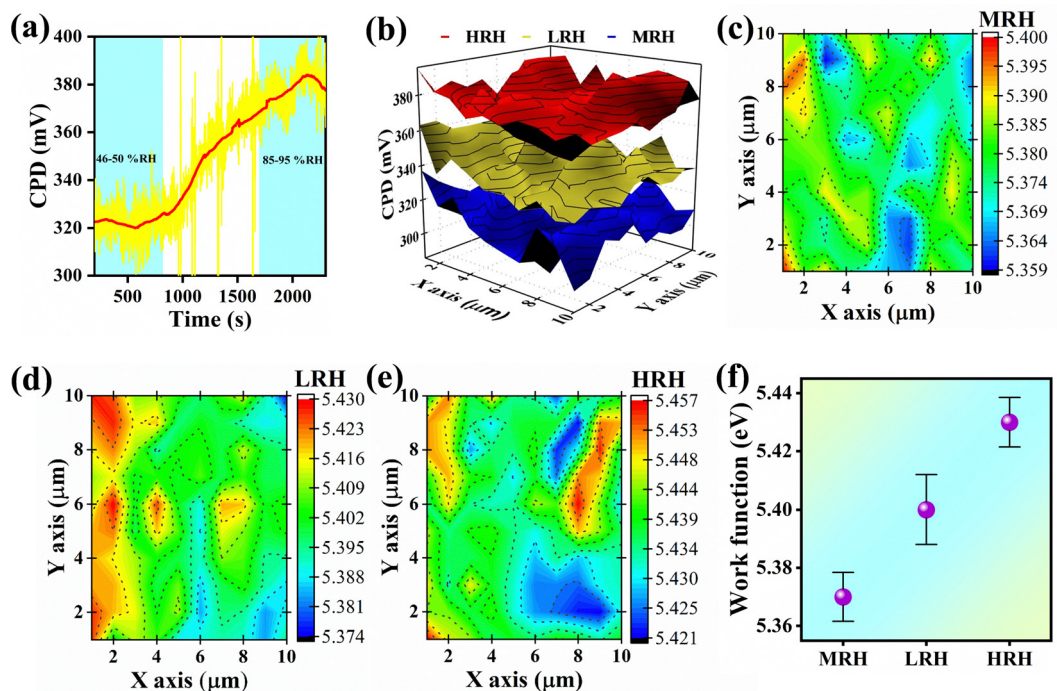
Fig. 6 (a) Dynamic CPD change with respect to RH, (b) corresponding 3D raster scan CPD measurement, (c)–(e) 2D scan images, and (f) work function distribution.
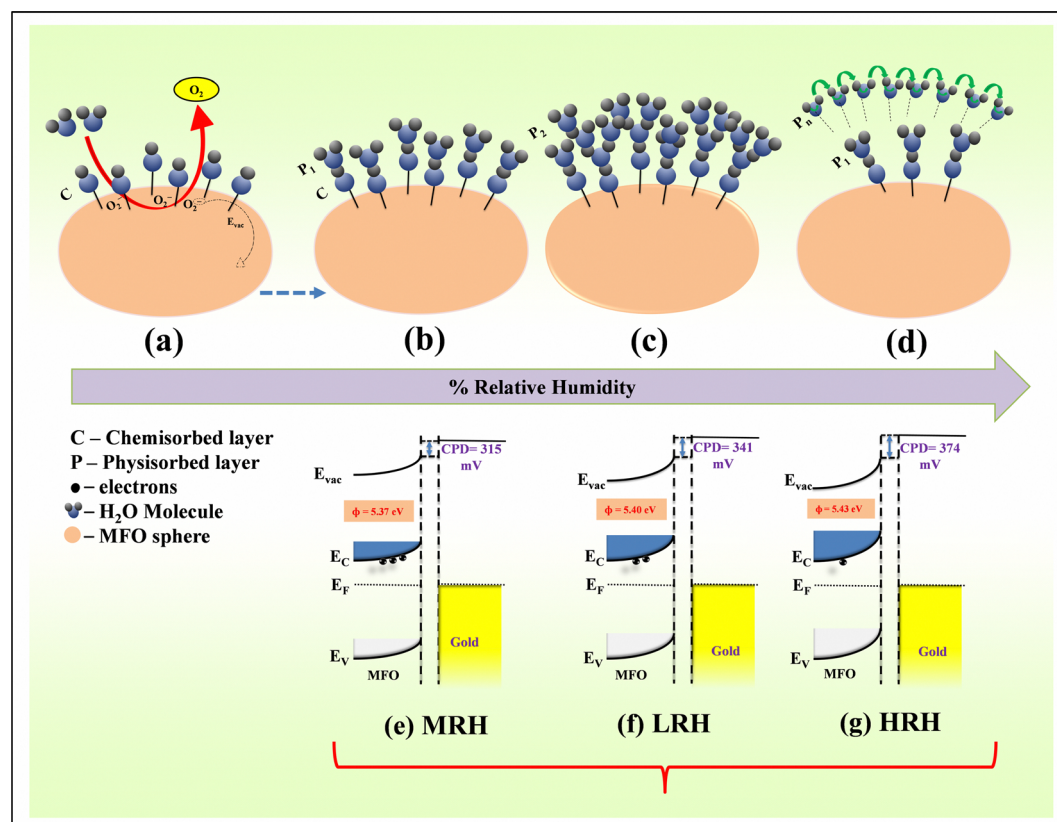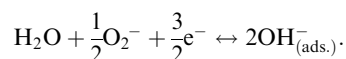

Fig. 7 (a)–(d) Schematic of the adsorption of water layers on the MFO surface and band configuration at (e) MRH, (f) LRH and (g) HRH.

molecules at room temperature using the following reaction:[55]

$$H_2O + \frac{1}{2}O_2^- + \frac{3}{2}e^- \leftrightarrow 2OH_{(ads.)}^-.$$

The water dissociation releases the electrons to the conduction band of the MFO to reduce resistance. This water dissociation process regulates the formation of the chemical OH^- layer above the MFO surface and metal ($M_{bulk} + H_2O \rightarrow M-OH^- + H^+$) (Fig. 7(a)). This process is called the chemisorption process, and the formed OH^- layer is the chemisorbed layer (Fig. 7(a)). This chemisorbed layer is not further reformed or affected by extra humidity and is difficult to remove.[49,51] Further increase in water molecules begins to form a physisorbed water layer above the chemisorbed surface. In this layer, conduction occurs owing to protonic (H^+) hoping by applying the Grotthuss chain mechanism ($H^+ + H_2O \rightarrow H_2O + H^+$).[55,56] The released hydrogen ion (H^+) hops through the chemisorbed OH^- and the first physisorbed layer. At low humidity, a lower concentration of water vapour leads to uneven occupancy of water molecules throughout the area. Thus, less proton hopping occurs, affecting the response of the sensor at lower humidity.

Furthermore, at higher humidity concentrations, the incoming H^+ ion protonates another water molecule to form hydronium (H_3O^+) ions ($H^+ + H_2O \rightarrow H_3O^+$). In the presence of an electric field, protons from the hydronium ion can easily hop across oxygen-lone pairs of water. Water molecules undergo protonation owing to oxygen with a single pair of electrons.[57] The process begins to generate multiple physisorbed layers onto the chemisorbed surface (Fig. 7(b)–(d)). In the upcoming stages, conduction occurs owing to the free and fast hopping of H^+ ions (Grotthus rearrangement chain).[57,58]

Further, from SKP measurements, it was clear that increasing % RH increased the ϕ. The SKP working principle is based on two parallel plate capacitors (when two dissimilar materials with different ϕ are close to each other, they try to create charge saturation between them by the transfer of electrons from the material with a lower ϕ to that with a higher ϕ).[40,59] In this study, the conducting Au tip had ϕ 5.1 eV while ϕ of n-type MFO was found at 5.37 eV, 5.40 eV and 5.43 eV in MRH, LRH and HRH, respectively; hence, the band bends upside at the edge, as shown in Fig. 7(e)–(g). The increase in work function relative to RH confirmed that water adsorption on the MFO stopped the emission of electrons out of the surface. The results are completely consistent with the earliest published article.[60] According to the Grotthus chain process (described above), the increase in RH caused the physisorbed layers to increase on the chemisorbed surface, which may, in turn, make a hindrance trap to emit electrons from the MFO. From the discussion, it can be concluded that the humidity concentration in the air can directly affect the material's ϕ.

4. Sensor testing in real life samples

The developed sensor was tested with wet and dry tissue paper, an index finger with and without hand glows, a wet finger, and finally the palm area of the hand. The influence of the above objects on the resistance of the sensor was dynamically investigated (Fig. S4, ESI†). Every component showed an obvious
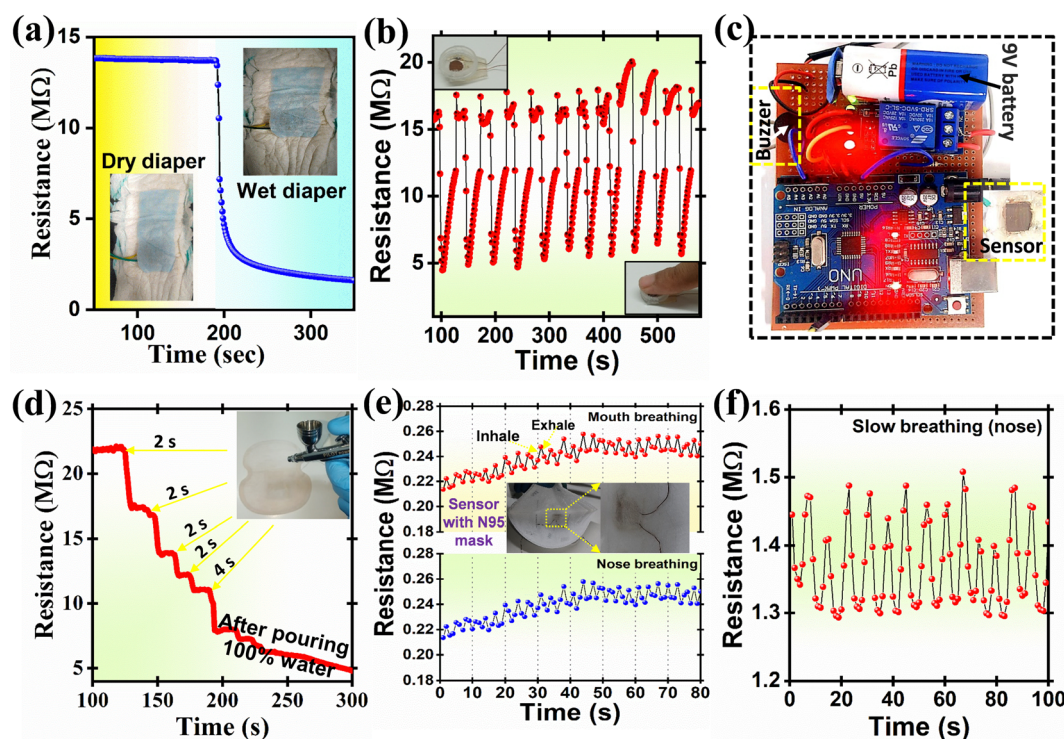

Fig. 8 (a) Response test in baby diaper, (b) finger humidity response test for contactless doorbell (or switch), (c) circuit arrangement, (d) sweat pad wetness response for various spraying steps, (e) mouth and nose breathing response in N95 mask, and (f) response for slow breathing test.

response. By contemplating the sensor's results, it was employed for the baby diaper wetness testing (Fig. 8(a)), finger humidity test for the contactless switch (or doorbell) (Fig. 8(b)), sweat control in the underarm sweat pad (Fig. 8(d)), breath monitoring (Fig. 8(e) and (f)), and skin humidity sensing (Fig. 9).

For baby diaper wetness testing, the PDMS encapsulated sensor (Fig. S5, ESI†) was inserted under the first cotton layer of the baby diaper with face direction downward (Fig. 8(a)); the humidity at this instance was measured to be ∼13 MΩ. However, upon pouring the tap water the resistance of the material suddenly falls to 5 MΩ within ∼10 s and 2.8 MΩ in 20 s, this result exhibits good response time. The above dynamic sensor measurement results showed good sensibility in the baby diaper. The data from the humidity sensor were acquired with an Arduino Uno micro-controller board and were further processed with custom-prepared 'C-program' code to reduce noise and obtain a smooth signal. The data were then monitored with a serial plotter, and the sensor output was used to control an external buzzer. The circuit for data acquisition consisted of one of the electrodes of the humidity sensor connected to the 3.3 V terminal of the microcontroller through a 10 kΩ resistor and the other end connected to the analogue input A3. The state of the buzzer was controlled using a 5 V relay. The entire device was powered by a 9 V DC battery (Fig. 8(c) and Movie S1, ESI†). Further, the sensor was tested at finger humidity in the context of contactless switches or doorbells (Fig. 8(b)); for this purpose, the fabricated sensor was fixed into a small pipe with a diameter 1 cm and a height ∼4 mm to avoid direct contact with a finger (inset Fig. 8(b)). The sensor response was tested in a laboratory atmosphere. The sensor showed a notable response before and after applying the figure to it (Fig. 8(b)). Using the Internet of Things (IoT)* interface, humidity can be monitored using mobile phones or any other suitable IoT device from a remote location.

The fabricated thick film sensor was then inserted into the first layer of the sweat pad and water was blasted into it using a spray pistol for 2 s, four times, to assess the moisture of the underarm sweat pad. The spraying of water obviously lowers the sensor's resistance, as shown in Fig. 8(d). The current results demonstrate that the sensor can be useful for
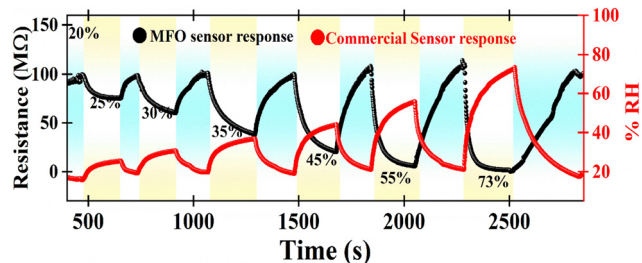

Fig. 10 Comparative response study of the MFO humidity sensor using a commercial humidity sensor (HygroClip-2 advanced series HC2A-S).

measuring human perspiration and can further be extended to measure animal and plant perspiration rates.

Additionally, a humidity sensor was attached to a mask (N95) to detect the rate of human breathing. In rare instances, such as during strenuous activity (exercise and heavy work), during chronic cough (colds and infections), and in some medical conditions, humans try to breathe through the mouth instead of a nose. It is necessary to assess the humidity sensor's response for mouth and nose breathing separately because the RH of air exhaled through the mouth is often higher than that of air exhaled through the nose owing to saliva. Fig. 8(e) shows how mouth breathing caused a greater resistance change ($\Delta R_{av.}$ = 14 806 Ω) than nose breathing ($\Delta R_{av.}$ = 11 738 Ω). This test offered evidence that the humidity sensor can accommodate 12–16 breaths per minute, which is the average breathing rate. Slow- and long-range breathing were also tested, and the results are shown in Fig. 8(f).

Human skin's water content is an essential factor to consider when assessing one's health and skin disorders.[61] However, human skin lacks receptors for detecting humidity. Mechanoreceptors and thermoreceptors can detect changes in humidity.[62] As illustrated in Fig. 9(a), the sensor was installed in three layers of flexible polyester transparent (PET) film for improved flexibility. For dry skin, the resistance of the humidity sensor was ∼8 MΩ (Fig. 9(b)). After working out (warming up and running for about an hour), the humidity sensor's resistance decreased to 116 kΩ. These findings show that the humidity sensor can be used to measure skin wetness and humidity and may be useful for assessing the moisturizing abilities of skincare products.

Fig. 10 depicts the sensor response comparison plot between the MFO humidity sensor and the commercial HygroClip 2 advanced series HC2A-S. The fabricated MFO sensor shows a consistent response towards each humidity level. Our results prove that the MFO humidity sensor can be an alternative to highly expensive commercial humidity sensors. The performance of MFO sensor characteristics can be further improved by applying a waterproof polyethene filter and appropriate non-degradable (gold/platinum) electrodes with miniaturised circuitry.

5. Conclusion

A uniformly distributed MFO with spherical morphology was prepared using the one-pot solvothermal technique. The
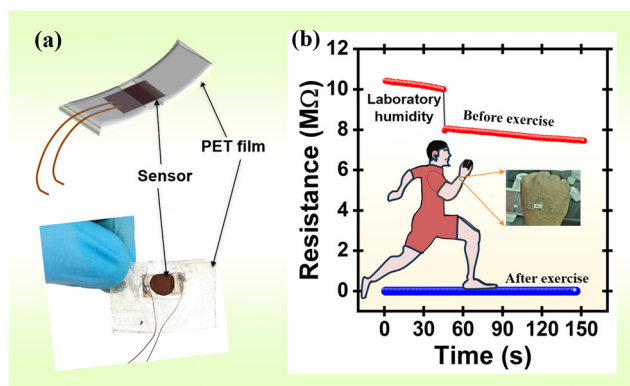

Fig. 9 (a) Schematic of the humidity sensor mounted on a PET film and (b) a real-time change in skin moisture resistance before and after exercise.

FESEM image shows a microsphere that contains numerous MFO nanoparticles. The wide range humidity sensing performance of MFO was investigated in dynamic (20 to 70% RH) and static methods (11 to 85% RH). The results proved that the MFO showed good sensitivity, detection resolution, and hysteresis. The effect of humidity concentration on changes in the work function of the sensing electrode was investigated using SKP. The ϕ is revealed to be directly proportional to the % RH level, and it increases gradually with respect to % RH. This study shows the effect of humidity on resistance and proves that % RH highly influences the material's work function. Finally, the fabricated sensor was successfully employed as a baby diaper alarm, finger humidity testing for contactless doorbells, human breath rate measurement, sweat pad humidity measurement, *etc.*

Author contributions

Conflicts of interest

The authors declare no competing financial interest.

Acknowledgements

References

1 I. Campero-Jurado, S. Márquez-Sánchez, J. Quintanar-Gómez, S. Rodríguez and J. M. Corchado, *Sensors*, 2020, **20**, 6241.

2 M.-C. Jeong and J. Kim, *Int. J. Environ. Res. Public Health*, 2019, **16**, 2984.

3 X. Wang, Y. Deng, X. Chen, P. Jiang, Y. K. Cheung and H. Yu, *Microsyst. Nanoeng.*, 2021, **7**, 1–11.

4 M. Zhang, M. Wang, M. Zhang, L. Qiu, Y. Liu, W. Zhang, Y. Zhang, J. Hu and G. Wu, *Nanomaterials*, 2019, **9**, 1399.

5 P. Chaudhary, D. K. Maurya, A. Pandey, A. Verma, R. K. Tripathi, S. Kumar and B. C. Yadav, *Sens. Actuators, B*, 2022, **350**, 130818.

6 K. Xu, Y. Fujita, Y. Lu, S. Honda, M. Shiomi, T. Arie, S. Akita and K. Takei, *Adv. Mater.*, 2021, **33**, 2008701.

7 Z. Duan, Y. Jiang, M. Yan, S. Wang, Z. Yuan, Q. Zhao, P. Sun, G. Xie, X. Du and H. Tai, *ACS Appl. Mater. Interfaces*, 2019, **11**, 21840–21849.

8 M. Zhang, S. Guo, D. Weller, Y. Hao, X. Wang, C. Ding, K. Chai, B. Zou and R. Liu, *Nanobiotechnology*, 2019, **17**, 1–10.

9 C. M. Furqan, M. U. Khan, M. Awais, F. Jiang, J. Bae, A. Hassan and H.-S. Kwok, *Sci. Rep.*, 2021, **11**, 1–14.

10 H. Yin, Y. Cao, B. Marelli, X. Zeng, A. J. Mason and C. Cao, *Adv. Mater.*, 2021, **33**, 2007764.

11 H. Bi, K. Yin, X. Xie, J. Ji, S. Wan, L. Sun, M. Terrones and M. S. Dresselhaus, *Sci. Rep.*, 2013, **3**, 1–7.

12 Z. Duan, Y. Jiang, Q. Zhao, Q. Huang, S. Wang, Y. Zhang, Y. Wu, B. Liu, Y. Zhen and H. Tai, *Sens. Actuators, B*, 2021, **339**, 129884.

13 R. S. Priya, P. Chaudhary, E. R. Kumar, A. Balamurugan, C. Srinivas, G. Prasad, B. C. Yadav and D. L. Sastry, *Ceram. Int.*, 2021, **47**, 15995–16008.

14 R. S. Ghuge, M. D. Shinde and S. B. Rane, *J. Electron. Mater.*, 2021, **50**, 6060–6072.

15 Y. Zhang, W. Zhang, Q. Li, C. Chen and Z. Zhang, *Sens. Actuators, B*, 2020, **324**, 128733.

16 M. Chen, S. Xue, L. Liu, Z. Li, H. Wang, C. Tan, J. Yang, X. Hu, X.-F. Jiang and Y. Cheng, *Sens. Actuators, B*, 2019, **287**, 329–337.

17 T.-G. Kang, J.-K. Park, G.-H. Yun, H. H. Choi, H.-J. Lee and J.-G. Yook, *Sens. Actuators, B*, 2019, **282**, 145–151.

18 L. Wang, J. Xu, X. Wang, Z. Cheng and J. Xu, *Sens. Actuators, B*, 2019, **288**, 289–297.

19 P. Shankar and J. B. B. Rayappan, *Sci. Lett. J.*, 2015, **4**, 126.

20 A. Šutka and K. A. Gross, *Sens. Actuators, B*, 2016, **222**, 95–105.

21 G. Xian, S. Kong, Q. Li, G. Zhang, N. Zhou, H. Du and L. Niu, *Front. Chem.*, 2020, **8**, 177.

22 M. Aghajanzadeh, E. Naderi, M. Zamani, A. Sharafi, M. Naseri and H. Danafar, *Drug Dev. Ind. Pharm.*, 2020, **46**, 846–851.

23 R. G. D. Andrade, S. R. S. Veloso and E. Castanheira, *Int. J. Mol. Sci.*, 2020, **21**, 2455.

24 Y. Shen, L. Wang, Y. Wu, X. Li, Q. Zhao, Y. Hou and W. Teng, *Catal. Commun.*, 2015, **68**, 11–14.

25 X. Lin, X. Lv, L. Wang, F. Zhang and L. Duan, *Mater. Res. Bull.*, 2013, **48**, 2511–2516.

26 S. Sharifi, K. Rahimi and A. Yazdani, *Sci. Rep.*, 2021, **11**, 1–15.

27 Z. Zhang, Y. Wang, Q. Tan, Z. Zhong and F. Su, *J. Colloid Interface Sci.*, 2013, **398**, 185–192.

28 Z. Liu, G. Chen, F. Hu and X. Li, *J. Environ. Manage.*, 2020, **263**, 110377.

29 L. Zhen, K. He, C. Y. Xu and W. Z. Shao, *J. Magn. Magn. Mater.*, 2008, **320**, 2672–2675.

30 Y. Liu, H. Liu, X. Zhao, L. Wang and G. Liang, *J. Wuhan Univ. Technol., Mater. Sci. Ed.*, 2019, **34**, 549–557.

31 L. Zhang, G. Wang, F. Yu, Y. Zhang, B.-C. Ye and Y. Li, *Sens. Actuators, B*, 2018, **258**, 589–596.

32 V. Nagarajan and A. Thayumanavan, *Appl. Surf. Sci.*, 2018, **428**, 748–756.

33 S. Sahoo, P. K. Sahoo, A. Sharma and A. K. Satpati, *Sens. Actuators, B*, 2020, **309**, 127763.

34 D. Deivatamil, M. M. J. Abel, S. Sivaranjani, R. Thiruneelakandan and J. J. Prince, *Inorg. Chem. Commun.*, 2021, **127**, 108546.

35 D. Deivatamil, J. A. M. Mark, T. Raghavan and J. P. Jesuraj, *Inorg. Chem. Commun.*, 2021, **123**, 108355.

36 S. Nilmoung, P. Kidkhunthod and S. Maensiri, *Mater. Chem. Phys.*, 2018, **220**, 190–200.

37 L. Song, C. Yan, W. Zhang, H. Wu, Z. Jia, M. Ma, J. Xie, N. Gu and Y. Zhang, *J. Nanomater*, 2016, **2016**, 4878935–4878943.

38 M. E. Mazhar, G. Faglia, E. Comini, D. Zappa, C. Baratto and G. Sberveglieri, *Sens. Actuators, B*, 2016, **222**, 1257–1263.

39 G. Marappan, E. Manoharan, D. Chidambaram, A. Kandasamy, Y. Sivalingam, C. di Natale and V. J. Surya, *Surf. Interfaces*, 2021, **27**, 101507.

40 G. P. Kuppuswamy, K. Pushparaj, V. J. Surya, E. K. Varadharaj, S. S. Kumar, C. di Natale and Y. Sivalingam, *J. Mater. Chem. C*, 2022, **10**, 5345–5355.

41 A. D'Amico, C. Di Natale, R. Paolesse, A. Mantini, C. Goletti, F. Davide and G. Filosofi, *Sens. Actuators, B*, 2000, **70**, 254–262.

42 M. F. Afsar, M. A. Rafiq, A. Jamil, S. Fareed, F. Siddique, A. I. Y. Tok and M. M. ul Hasan, *ACS Omega*, 2019, **4**, 2030–2039.

43 W. Meng, S. Wu, X. Wang and D. Zhang, *Sens. Actuators, B*, 2020, **315**, 128058.

44 M. Sheng, L. Gu, R. Kontic, Y. Zhou, K. Zheng, G. Chen, X. Mo and G. R. Patzke, *Sens. Actuators, B*, 2012, **166**, 642–649.

45 G. K. Dutta, S. Kasthuri, G. Marappan, S. V. Jayaraman, Y. Sivalingam, C. Di Natale and V. Nutalapati, *J. Mater. Chem. C*, 2019, **7**, 9954–9965.

46 M. Elakia, M. Gobinath, Y. Sivalingam, E. Palani, S. Ghosh, V. Nutalapati and V. J. Surya, *Phys. E*, 2020, **124**, 114232.

47 N. S. Ramgir, P. K. Sharma, N. Datta, M. Kaur, A. K. Debnath, D. K. Aswal and S. K. Gupta, *Sens. Actuators, B*, 2013, **186**, 718–726.

48 Z.-H. Duan, Q.-N. Zhao, C.-Z. Li, S. Wang, Y.-D. Jiang, Y.-J. Zhang, B.-H. Liu and H.-L. Tai, *Rare Met.*, 2021, **40**, 1762–1767.

49 V. Manikandan, A. Mirzaei, S. Sikarwar, B. C. Yadav, S. Vigneselvan, A. Vanitha and J. Chandrasekaran, *RSC Adv.*, 2020, **10**, 13611–13615.

50 V. Manikandan, S. Sikarwar, B. C. Yadav and R. S. Mane, *Sens. Actuators, A*, 2018, **272**, 267–273.

51 Z. Wang, Y. Xiao, X. Cui, P. Cheng, B. Wang, Y. Gao, X. Li, T. Yang, T. Zhang and G. Lu, *ACS Appl. Mater. Interfaces*, 2014, **6**, 3888–3895.

52 P. P. Hankare, S. D. Jadhav, U. B. Sankpal, R. P. Patil, R. Sasikala and I. S. Mulla, *J. Alloys Compd.*, 2009, **488**, 270–272.

53 M. Zhuo, Y. Chen, J. Sun, H. Zhang, D. Guo, H. Zhang, Q. Li, T. Wang and Q. Wan, *Sens. Actuators, B*, 2013, **186**, 78–83.

54 H. Wang, M. Zhao, W. Zhu, Z. Liu, G. Wang, S. Tang, D. Chen, J.-M. Lee, S. Yang and G. Ding, *Mater. Lett.*, 2020, **277**, 128343.

55 D. Burman, S. Santra, P. Pramanik and P. K. Guha, *Nanotechnology*, 2018, **29**, 115504.

56 B. P. Dhonge, S. S. Ray and B. Mwakikunga, *RSC Adv.*, 2017, **7**, 21703–21712.

57 S. N. Patil, A. M. Pawar, S. K. Tilekar and B. P. Ladgaonkar, *Sens. Actuators, A*, 2016, **244**, 35–43.

58 X. Peng, L. Hu, F. Qin, Y. Zhou and P. K. Chu, *Adv. Mater. Interfaces*, 2018, **5**, 1701404.

59 V. Palermo, M. Palma and P. Samorì, *Adv. Mater.*, 2006, **18**, 145–164.

60 M. Xue, J. Xie, W. Li, C. Yang, Y. Ai, F. Wang, J. Ou and J. Yao, *Physica B*, 2011, **406**, 4240–4244.

61 T. Li, L. Li, H. Sun, Y. Xu, X. Wang, H. Luo, Z. Liu and T. Zhang, *Adv. Sci.*, 2017, **4**, 1600404.

62 Q. Hua, J. Sun, H. Liu, R. Bao, R. Yu, J. Zhai, C. Pan and Z. L. Wang, *Nat. Commun.*, 2018, **9**, 244.